

Welding-Induced Microstructure Evolution of a Cu-Bearing High-Strength Blast-Resistant Steel

JEREMY L. CARON, SUDARSANAM SURESH BABU, and JOHN C. LIPPOLD

A new high strength, high toughness steel containing Cu for precipitation strengthening was recently developed for naval, blast-resistant structural applications. This steel, known as Blast-Alloy160 (BA-160), is of nominal composition Fe-0.05C-3.65Cu-6.5Ni-1.84Cr-0.6Mo-0.1V (wt pct). The evident solidification substructure of an autogenous gas tungsten arc (GTA) weld suggested fcc austenite as the primary solidification phase. The heat-affected zone (HAZ) hardness ranged from a minimum of 353 HV in the coarse-grained HAZ (CGHAZ) to a maximum of 448 HV in the intercritical HAZ (ICHAZ). After postweld heat treatment (PWHT) of the spot weld, hardness increases were observed in the fusion zone (FZ), CGHAZ, and fine-grained HAZ (FGHAZ) regions. Phase transformation and metallographic analyses of simulated single-pass HAZ regions revealed lath martensite to be the only austenitic transformation product in the HAZ. Single-pass HAZ simulations revealed a similar hardness profile for low heat-input (LHI) and high heat-input (HHI) conditions, with higher hardness values being measured for the LHI samples. The measured hardness values were in good agreement with those from the GTA weld. Single-pass HAZ regions exhibited higher Charpy V-notch impact toughness than the BM at both test temperatures of 293 K and 223 K (20 °C and -50 °C). Hardness increases were observed for multipass HAZ simulations employing an initial CGHAZ simulation.

DOI: 10.1007/s11661-011-0801-1

© The Minerals, Metals & Materials Society and ASM International 2011

I. INTRODUCTION

THE Office of Naval Research (ONR) and the Defense Advanced Research Projects Agency are focused on devising multiscale characterization and simulation techniques that lead to the development of optimized materials.^[1] These techniques span across multiple scientific disciplines and range in length scale from the atomic level to the macroscale, including atomistic modeling, three-dimensional digital microstructural reconstructions, phase-field modeling, and finite element modeling.^[2,3] In general, the studies have thus far only focused on wrought metals with carefully developed microstructures. To consider the microstructure evolution that occurs during welding, weldability testing techniques and advanced characterization of weld microstructures are being incorporated into these materials research programs.

Steels are currently the principal structural material in existing naval ships and submarines; this will continue to be the trend in the near future, given their relatively low cost, suitable combination of mechanical properties, and existing infrastructure for their processing and

fabrication.^[3] Research is currently directed toward developing steels with high toughness for ballistic impact resistance in combination with high strength levels. The specific room-temperature property requirements for high-strength blast-resistant steels are yield strengths of 1030 to 1240 MPa and Charpy V-notch impact toughness values above 115 J.^[4,5]

BlastAlloy160 (BA-160) is one such alloy that was developed to meet the property requirements for blast-resistant naval material applications.^[4,5] This alloy design initiative was in part prompted by the terrorist attack on the Navy destroyer USS Cole in 2000.^[6,7] The BA-160 alloy is a high-strength transformation-toughened steel developed at Northwestern University using a theoretical computational materials design concept. The nominal chemical composition of BA-160 is Fe-0.05C-3.65Cu-6.5Ni-1.84Cr-0.6Mo-0.1V (wt pct). A minimum yield strength of 1103 MPa is provided by very fine (3 to 5 nm) Cu-rich precipitates and M₂C carbides (where M represents the elements Cr, Mo, and V) in a mixed martensitic/bainitic matrix. An impact toughness level of 176 J is attributed to dispersed phase transformation toughening, which is provided by Ni-stabilized austenite precipitates. Studies by the alloy design team were focused on determining the heat treatment providing the best combination of strength/hardness and toughness.^[5,8] The size refinement and compositional enrichment of the austenite precipitates is achieved through multistep tempering. The austenite is first nucleated in a fine form at a higher tempering temperature of 823 K (550 °C) for 30 minutes, followed by tempering at a lower temperature of 723 K (450 °C) for 5 hours to allow for Ni enrichment of the austenite precipitates.

JEREMY L. CARON, Graduate Research Associate, is with the Department of Materials Science and Engineering, Welding Engineering Program, The Ohio State University, Columbus, OH 43221, is now Welding Metallurgist, with the Research and Technology Group, Haynes International, Inc., Kokomo, IN 46904. Contact e-mail: jcaron@haynesintl.com SUDARSANAM SURESH BABU, Associate Professor, and JOHN C. LIPPOLD, Professor, are with the Department of Materials Science and Engineering, Welding Engineering Program, The Ohio State University.

Manuscript submitted January 4, 2011.

Article published online September 15, 2011

Additional toughness is also provided by precipitation of M_2C carbides, which replaces the brittle cementite (Fe_3C) phase during the tempering procedure.

In this investigation, testing was conducted to determine the nature of microstructure evolution in the fusion zone (FZ) and heat-affected zone (HAZ) of BA-160 during welding. These tests included welding experiments and physical simulations performed with the Gleeble*

*Gleeble is a trademark of Dynamic Systems, Inc., Poestenkill, NY.

thermal-mechanical simulator. The experimental results were supplemented by computational materials modeling predictions to better understand the welding-induced microstructure evolution of BA-160.

II. EXPERIMENTAL PROCEDURE

A. Material

The BA-160 experimental material was provided by QuesTek Innovations LLC (Evanston, IL). The measured chemical composition of BA-160 is provided in Table I. The steel was initially cast into 20.5-cm ingots by vacuum induction melting and vacuum arc remelting, followed by homogenization at 1477 K (1204 °C) for 12 hours. The ingots were then cogged to 8-cm round corner square billet and subsequently rotary forged to 4.1-cm diameter. The material was then normalized at 1183 K (910 °C) for 1 hour and heat treated at 755 K (482 °C) for 10 hours before being finish turned into 34.9-mm-diameter barstock. The final heat treatment procedure was performed on sections of the barstock using a model 7GT-K24 Lucifer box furnace (Lucifer

Table I. Measured Chemical Composition of BA-160 Experimental Material

Element	Wt Pct
C	0.059
Mn	0.001
Si	0.015
P	<0.005
S	<0.001
Cu	3.39
Ni	6.8
Cr	1.9
Mo	0.61
V	<0.001
Nb	<0.001
Ti	0.016

Furnaces, Inc., Warrington, PA). An argon atmosphere was used in the furnace chamber to protect the material from oxidation and decarburization. The details of the heat treatment procedure for BA-160 are outlined in Table II. Shown in Figure 1 is a light optical micrograph of the BA-160 base metal (BM) microstructure after the heat treatment procedure.

B. Welding Experiments

The choice of welding experiments were limited by the barstock form of the material. To provide an initial assessment of the microstructure evolution during welding of BA-160, a gas tungsten arc (GTA) spot weld was applied to a “puck” of fully heat-treated material. The puck dimensions were 34.9-mm diameter and 10-mm thickness. The spot weld was performed with a model 9027 Jetline side beam welder (Jetline Engineering, Irvine, CA). The spot weld parameters were arc current of 175 A and average arc voltage of 16.2 V, applied for 5.7 seconds with an arc gap of 6.35 mm. Argon gas shielding was set at $1.57 \times 10^{-4} \text{ m}^3/\text{s}$ (20 CFH) with a 5-second preflow and 30-second postflow to prevent oxidation.

To preserve the microstructure for subsequent post-weld heat treatment (PWHT) experiments and characterization, thermocouples were not plunged in the weld to determine the cooling rate. An estimate of the cooling rate was determined from equations developed for an instantaneous point heat source in a heavy slab.^[9] The applied welding parameters and the width of the “transformed” HAZ region heated above the A_{c1} ,



Fig. 1—Microstructure of BA-160 BM in the heat-treated condition with measured hardness of 402 HV.

Table II. Heat Treatment Procedure for BA-160

Step	Temperature [K (°C)]	Duration	$T \rightarrow T_{\text{ambient}}$
1. Austenitization	1173 (900)	1 h	water quench
2. Liquid nitrogen hold	77 (−196)	30 min	air warm
3. Primary tempering	823 (550)	30 min	water quench
4. Secondary tempering	723 (450)	5 h	air cool

measured to be 2.925 mm, were employed to calculate a $t_{8/5}$ value. The $t_{8/5}$ represents the cooling time from 1073 K to 773 K (800 °C to 500 °C), an established index of cooling rates in steel welds that influences phase transformation behavior. The estimated $t_{8/5}$ for the center of the spot weld was calculated to be 5.5 seconds. Since spot weld cooling rates within the weld zone are virtually identical to each other below 1073 K (800 °C), the calculated $t_{8/5}$ is also considered valid for positions relatively far away from the spot weld center, including the HAZ regions closest to the weld interface.^[9] The calculated $t_{8/5}$ is considered a reasonable estimate given that spot welds typically produce very fast cooling rates that are higher than those experienced in linear arc welds; the calculated value represents a lower bound of cooling time expected in an actual arc welding application. Cooling rates, as determined from plunged thermocouples in the weld metal, for subsequent spot weld experiments employing higher energy inputs confirmed that the calculated $t_{8/5}$ of 5.5 seconds was a realistic estimate of the weld cooling rate.

C. HAZ Simulations

The HAZ is considered to consist of both the “true” HAZ (T-HAZ) and the partially-melted zone (PMZ). The T-HAZ is distinguished as the region of the HAZ where all metallurgical reactions occur in the solid state. The PMZ represents the region of the HAZ adjacent to the weld interface where a transition from 100 pct liquid of the FZ to 100 pct solid of the T-HAZ occurs. In steels, the T-HAZ is further subdivided into characteristic regions that are loosely correlated to the Fe-C equilibrium phase diagram,^[10] as shown in Figure 2. The four characteristic regions are known as (1) the subcritical HAZ (SCHAZ), where no detectable transformation to austenite occurs below the A_{c1} temperature; (2) the intercritical HAZ (ICHAZ), where only partial transformation to austenite occurs between the

A_{c1} and A_{c3} temperatures; (3) the fine-grained HAZ (FGHAZ), where full transformation to austenite occurs at a peak temperature slightly above the A_{c3} temperature; and (4) the coarse-grained HAZ (CGHAZ), where full transformation to austenite occurs at a peak temperature much above the A_{c3} temperature.

The characteristic T-HAZ regions of BA-160 were investigated using thermal simulations in a similar approach to previous studies of naval steels.^[11,12] The simulations were performed with the Gleeble 3800 thermal-mechanical simulator (Dynamic Systems, Inc., Poestenkill, NY). The peak temperatures of the HAZ simulations were selected in reference to the acquired dilatometry data and are provided in Table III for reference. The solid bar test samples were of 6.35-mm diameter and 101.6-mm length. The temperature was controlled with type K thermocouple wire, which was percussion welded at the midsection of the sample. The samples were heated to peak temperature at a linear rate of 100 K/s and held for 1 second before cooling to ambient temperature. Two weld cooling rates were simulated: (1) a faster cooling rate to simulate low heat-input (LHI) welding conditions with no preheat and (2) a slower cooling rate to simulate high heat-input (HHI) welding conditions with a moderate preheat temperature. The cooling rates were achieved through the selection of either copper or stainless steel grip sets, and through adjustment of the spacing between the

Table III. Selected Peak Temperatures for BA-160 Single-Pass HAZ Simulations

HAZ Region	Location	Peak Temperature [K (°C)]
SCHAZ	$T < A_{c1}$	923 (650)
ICHAZ	$A_{c1} < T < A_{c3}$	1023 (750)
FGHAZ	$T > A_{c3}$	1173 (900)
CGHAZ	$T \gg A_{c3}$	1573 (1300)

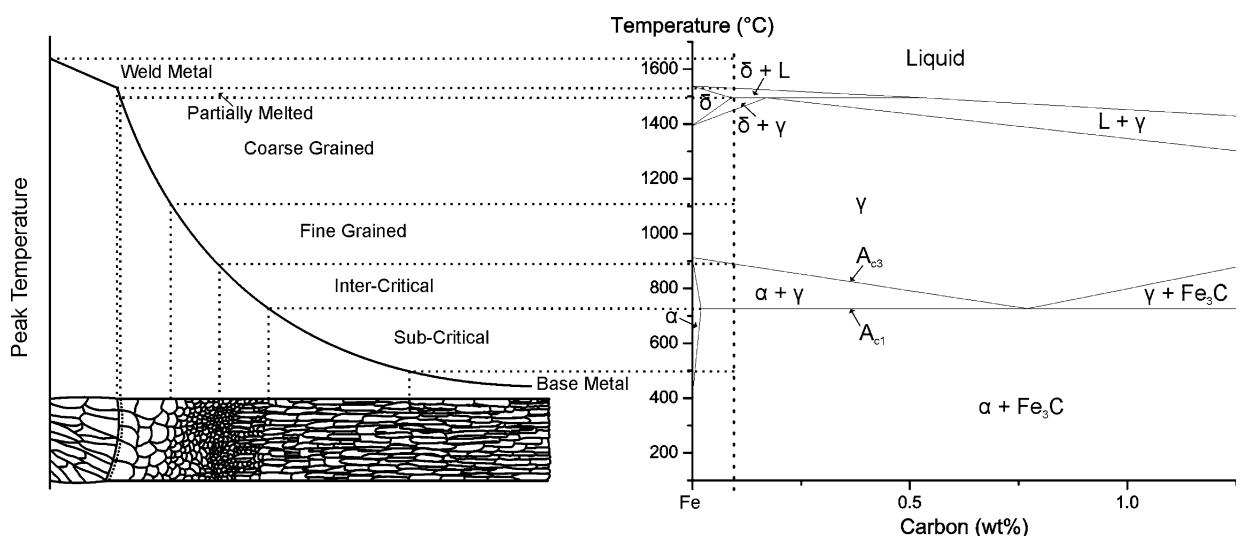


Fig. 2—Schematic illustration of the location of fusion weld regions observed in steels with respect to the Fe-Fe₃C equilibrium phase diagram. Fe-Fe₃C diagram calculated with THERMO-CALC software and TCBIN solutions database. Schematic adapted from Ref. 10.

grips, referred to as the “free span” of the sample. The average $t_{8/5}$ times were 10 and 45 seconds for the LHI and HHI simulations, respectively. The thermal cycles were conducted in a high vacuum (approximately 1.3×10^{-4} Pa) to limit sample surface oxidation and thermocouple detachment.

Following the single-pass HAZ simulations of BA-160, a limited number of multipass HAZ simulations were also conducted. In multipass welding, the single-pass HAZ regions are modified by subsequent thermal cycles, leading to a variety of localized and discontinuous microstructural regions. An understanding of how multiple thermal cycles affect the metallurgical properties of the various weld regions proves useful in tailoring the weld procedure for optimum properties without the need for PWHT, similar to a “temper bead” procedure.^[13] For consistency, the same peak temperatures were used as for the single-pass HAZ simulations. The multipass simulations evaluated a moderate cooling rate that provided an approximate $t_{8/5}$ of 15 seconds.

The phase transformation temperatures during the HAZ simulations were determined using both dilatometry and single sensor-differential thermal analysis (SS-DTA) techniques.^[14] Dilatometry is a well-established technique for determining phase transformation temperatures in steels.^[15,16] When an alloy undergoes a phase transformation, the change in lattice structure that may accompany the phase transformation and result in a change in specific volume is accurately determined by a dilatometer positioned on the specimen. During the simulations, these data allowed the determination of the A_{c1} and A_{c3} temperatures, the on-cooling phase transformation temperatures, and the fraction of austenite transformed as a function of temperature. The SS-DTA technique uses a single temperature acquisition and a calculated reference thermal cycle to determine phase transformation temperatures.^[14] The reference thermal history is calculated by analytical formulas or by modeling of the heat flow in the tested sample. The thermal effect of the phase transformation is revealed through a deviation in ΔT between the measured and reference curves. The deviations in the T vs ΔT curve indicate the start and finish temperatures of the phase transformations. In order to perform the SS-DTA technique, it was necessary that the samples be “free cooled” in the Gleeble, *i.e.*, without power angle heating to provide cooling rate control.

D. Charpy V-Notch Impact Testing

The toughness of single-pass HAZ samples was investigated using the Charpy V-notch impact test. The representative regions of the HAZ were first simulated in the Gleeble using unnotched Charpy “blanks.” The temperature was controlled with type K thermocouple wire, which was percussion welded at the midsection of the sample. Samples were heated at 100 K/s to the same peak temperatures as for the single-pass HAZ simulations (Table III) and cooled to ambient temperature at a moderate cooling rate ($t_{8/5}$ = 15 seconds) in a high vacuum atmosphere. In order to

maximize the available material, subsize (5 mm × 5 mm × 55 mm) specimens were employed. Following the HAZ simulations, notches were machined in the sample blanks. The specimen and notch geometry were in accordance with ASTM Designation E 23,^[17] notch geometry consisted of a 45 deg center notch of depth 1 mm and root radius 25 mm. The impact tests were conducted with a 81 J capacity P1-2 model Riehle Testing Machine. Samples were tested at an ambient temperature of 293 K (20 °C) to provide a baseline toughness value and at 223 K (−50 °C) to investigate the toughness response at lower temperatures. The impact energy values of BM samples were also determined to provide both a comparative toughness baseline for the HAZ samples and a reference to values reported for the prototype alloy by Saha *et al.*^[5] using standard size (10 mm × 10 mm × 55 mm) specimens. For the 223 K (−50 °C) tests, the samples were cooled to the test temperature by immersion in a solution of acetone and dry ice. The samples were held in the solution for 10 minutes to stabilize the temperature and then promptly tested following removal from the solution. Due to limited material availability, only two samples were evaluated at each test temperature to determine an average value. Adjusted impact energy values, E_{adj} , were derived from the idealized nominal fracture volume equation, $[Bb]^{3/2}$, where B is the specified width of the sample and b is the ligament thickness below the notch root.^[18,19] The specimen length and notch geometry are not considered in the formula, since they are equivalent for both the standard and subsize Charpy specimens.

E. Microstructure Characterization

After testing, samples selected for metallographic analysis were sectioned using a precision diamond saw and mounted in either thermoset or conductive mounting powders. Following mounting, samples were ground successively with 240, 320, 400, 600, and 800 grit SiC papers. Rough polishing was performed with 3- μ m diamond particles. Final polishing consisted of 1- and 0.05- μ m alumina aqueous solutions. In between each polishing step, the samples were cleaned using detergent and water and dried with hot air. Sample etching was performed with 2 and 5 pct Nital etchants, applied with a cotton swab directly to the sample surface. The presence and distribution of retained austenite was revealed with an etching technique consisting of a pre-etch with 2 pct Nital followed by immersed etching in 10 pct aqueous sodium metabisulfite.^[20,21] The prior austenite grains in the HAZ were revealed using a color etchant solution consisting of 50 mL distilled water, 50 g $\text{Na}_2\text{S}_2\text{O}_3 \cdot 5\text{H}_2\text{O}$, and 5 g $\text{K}_2\text{S}_2\text{O}_5$. The sample was immersed in the etchant for 5 to 10 minutes and then lightly polished with 0.05- μ m alumina aqueous solution. The average prior austenite grain diameters of the single-pass HAZ samples were then determined using the linear intercept method of ASTM Designation E 112.^[22] Light optical micrographs were acquired using an Olympus GX-51 inverted metallurgical microscope equipped with an Olympus DP71 digital camera (Olympus Corporation, Tokyo, Japan). The micro-

hardness of test samples was determined manually, in accordance with ASTM Designation E 384,^[23] using a LECO** M-400-H1 hardness testing machine.

**LECO is a trademark of LECO Corporation, St. Joseph, MI.

Fracture surfaces of Charpy V-notch test samples were examined with a PHILIPS† XL-30 ESEM scanning

†PHILIPS is a trademark of FEI Company, Hillsboro, OR.

electron microscope. Fractographic samples were ultrasonically cleaned in ethyl alcohol, air dried, and then furnace baked before examination.

III. RESULTS AND DISCUSSION

A. Characterization of As-Welded Microstructures

The microstructure of the spot weld near the weld interface is shown in Figure 3. The interface between the HAZ and the solidified microstructure, herein referred to as the “fusion” zone (FZ), is clearly demarcated by the remnants of the cellular/dendritic solidification substructure of the FZ. The readily apparent solidification substructure of the weld microstructure is indicative that primary solidification occurred as the face-centered-cubic (fcc) austenite phase. Since the diffusivity of alloying and impurity elements is typically much lower in fcc austenite compared to bcc ferrite, stronger chemical segregation can be expected in the last liquid to solidify in fcc austenite weld metal, preserving the segregation profile that develops during solidification.^[24] Scheil solidification simulations performed with the THERMO-CALC‡ software^[25]

‡THERMO-CALC is a trademark of Thermo-Calc Software, Stockholm, Sweden.

and TCFE5 thermodynamic solutions database also predicted austenite as the primary solidification phase. This finding is attributed to the relatively high Ni content, a strong austenite-stabilizing element. This is a potentially important characteristic of this alloy, since primary austenite solidification in conjunction with a wide solidification temperature range is associated with increased solidification cracking susceptibility relative to solidification as bcc delta-ferrite.

Identified in Figure 3 are three major types of boundaries that were observed near the weld interface. A solidification subgrain boundary separates adjacent subgrains (cells and dendrites) in the weld. The boundary between packets of subgrains is known as a solidification grain boundary (SGB). Also identifiable are prior austenite grain boundaries in the HAZ region near the weld interface. In certain locations at the weld interface, the prior austenite grain boundaries were observed to link up with the SGBs of the weld microstructure, implying continuous chemical segregation across the weld interface

according to a pipeline diffusion mechanism.^[26] The etching characteristics of the prior austenite grain boundaries also suggest the presence of a PMZ consisting of liquid formed along the austenite grain boundaries nearest to the weld interface where the highest peak temperatures are experienced.

The Vickers microhardness traverse across the as-welded puck is shown in Figure 4. The average hardness of the FZ was found to be 364 HV. In the HAZ, a minimum hardness value of 353 HV was measured directly adjacent to the weld interface, gradually increasing to a maximum value of 448 HV before a sharp decrease to 387 HV near the BM. The maximum hardness in the HAZ was noted to occur in the microstructural region heated just above the A_{c1} , *i.e.*, the ICHAZ, which was denoted by a sharp microstructural contrast with the BM due to austenite formation. Through microstructural observations, the average hardness of each HAZ region was estimated from the measured values, as summarized in Table IV.

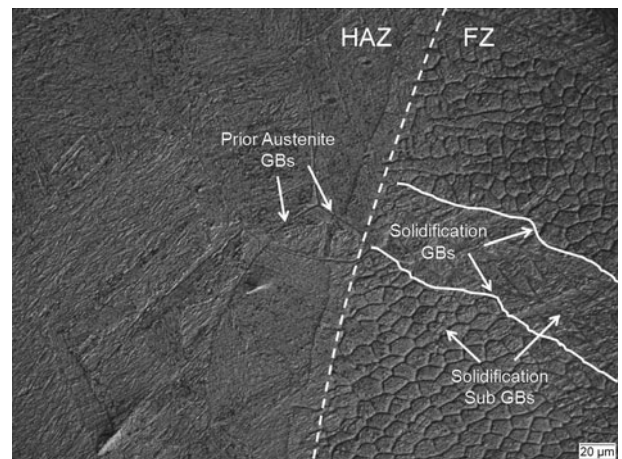


Fig. 3—Microstructure of the BA-160 spot weld near the weld interface with microstructural boundaries identified. Imaged using differential interference contrast microscopy.

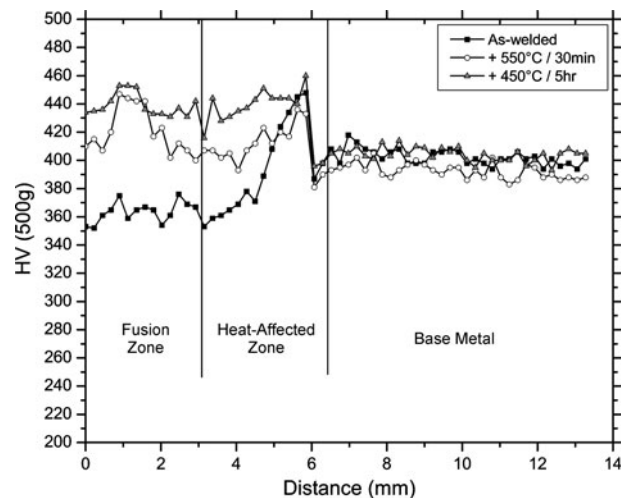


Fig. 4—Vickers microhardness traverses across the BA-160 spot weld in the as-welded condition and after each step of PWHT.

Table IV. Summary of Average Vickers Microhardness Values for Microstructural Regions of BA-160 Spot Weld in As-Welded Condition and After Each Step of the PWHT Procedure

Step	Vickers Microhardness					
	FZ	CGHAZ	FGHAZ	ICHAZ	SCHAZ	BM
As-welded	364	360	383	438	398	402
+ 823 K (550 °C)/30 min	421	405	409	427	390	392
+ 723 K (450 °C)/5 h	439	430	442	447	402	404

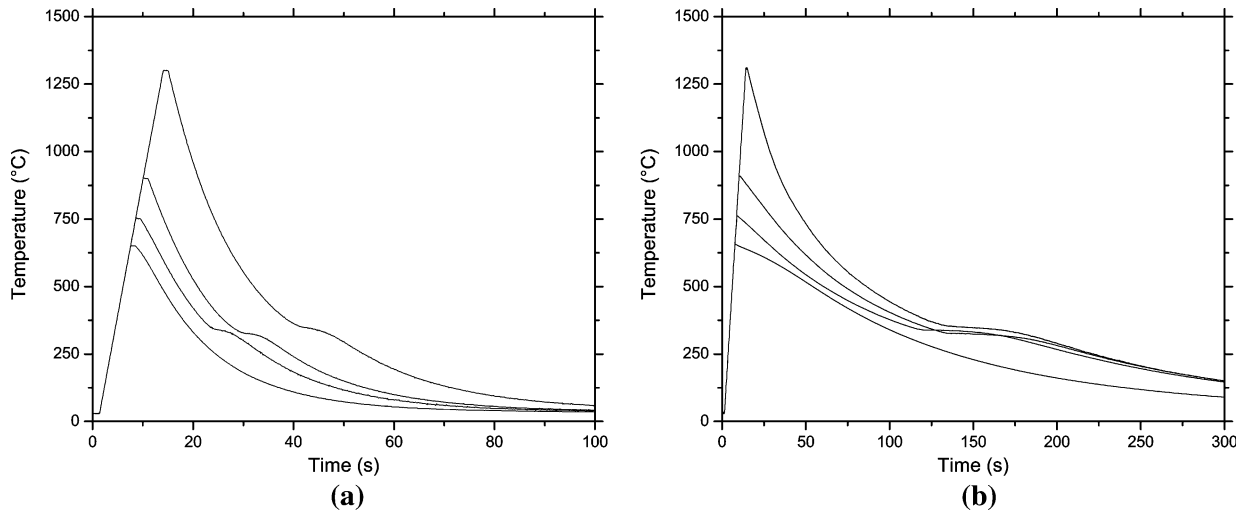


Fig. 5—Acquired thermal profiles of BA-160 single-pass HAZ simulations for (a) LHI conditions and (b) HHI conditions.

B. PWHT Analysis

To investigate the hardness response of the BA-160 weld regions during PWHT, the puck was heat treated according to the two-step tempering procedure developed for the BM. Thus, the first step of the PWHT involved tempering at 823 K (550 °C) for 30 minutes followed by water quenching. The second step consisted of a 5-hour temper at 723 K (450 °C) followed by air cooling. The BM tempering procedure was chosen simply as a first approximation of the PWHT response, clearly recognizing that a distinct PWHT (probably at a single temperature) is likely more appropriate for BA-160. Hardness traverses at a location near the location of the as-welded measurements were performed across the puck after each tempering step, as shown in Figure 4. Hardness increases were observed in the FZ, CGHAZ, and FGHAZ regions after initial tempering at 823 K (550 °C) for 30 minutes. The largest hardness increase was observed in the FZ with an increase from 364 to 421 HV. Following the second tempering step at 723 K (450 °C) for 5 hours, hardness increases were again observed in the FZ, CGHAZ, and FGHAZ regions, the largest increase from 409 to 442 HV being observed in the FGHAZ. The hardness of the ICHAZ also increased from 427 to 447 HV during the second tempering step. It is noted that the hardnesses of the SCHAZ and BM regions were not strongly affected by either tempering step. The larger hardness increases in the FZ, CGHAZ, and FGHAZ regions coincide with

the anticipated greater dissolution of precipitates and solutionizing of alloying elements during the on-heating portion of the weld thermal cycle at the higher peak temperatures. The supersaturation of Cu during the on-cooling portion of the weld thermal cycle, as predicted by the binary Fe-Cu equilibrium phase diagram, would be expected to promote the formation of Cu precipitates during subsequent tempering.^[27–31] Overall, the HAZ hardness values were comparable to or above the BM hardness following PWHT. A narrower range of hardness values was also observed after PWHT when compared to the as-welded condition. The relatively constant hardness observed across the weld regions following PWHT is considered a potential positive weldability aspect for this alloy. However, if the hardness increase is associated with strong precipitation reactions, BA-160 may exhibit reheat cracking susceptibility.

C. Phase Transformation Analyses of Single-Pass HAZ Regions

Shown in Figure 5 are the acquired thermal data for the LHI and HHI HAZ simulations. The thermal arrest that occurs during the cooling portion of the thermal cycle is indicative of the on-cooling phase transformation start temperature. Dilatometric analyses were used to determine the on-heating phase transformation temperatures. Plots acquired from dilatometry data are shown in Figure 6. The determination and verification

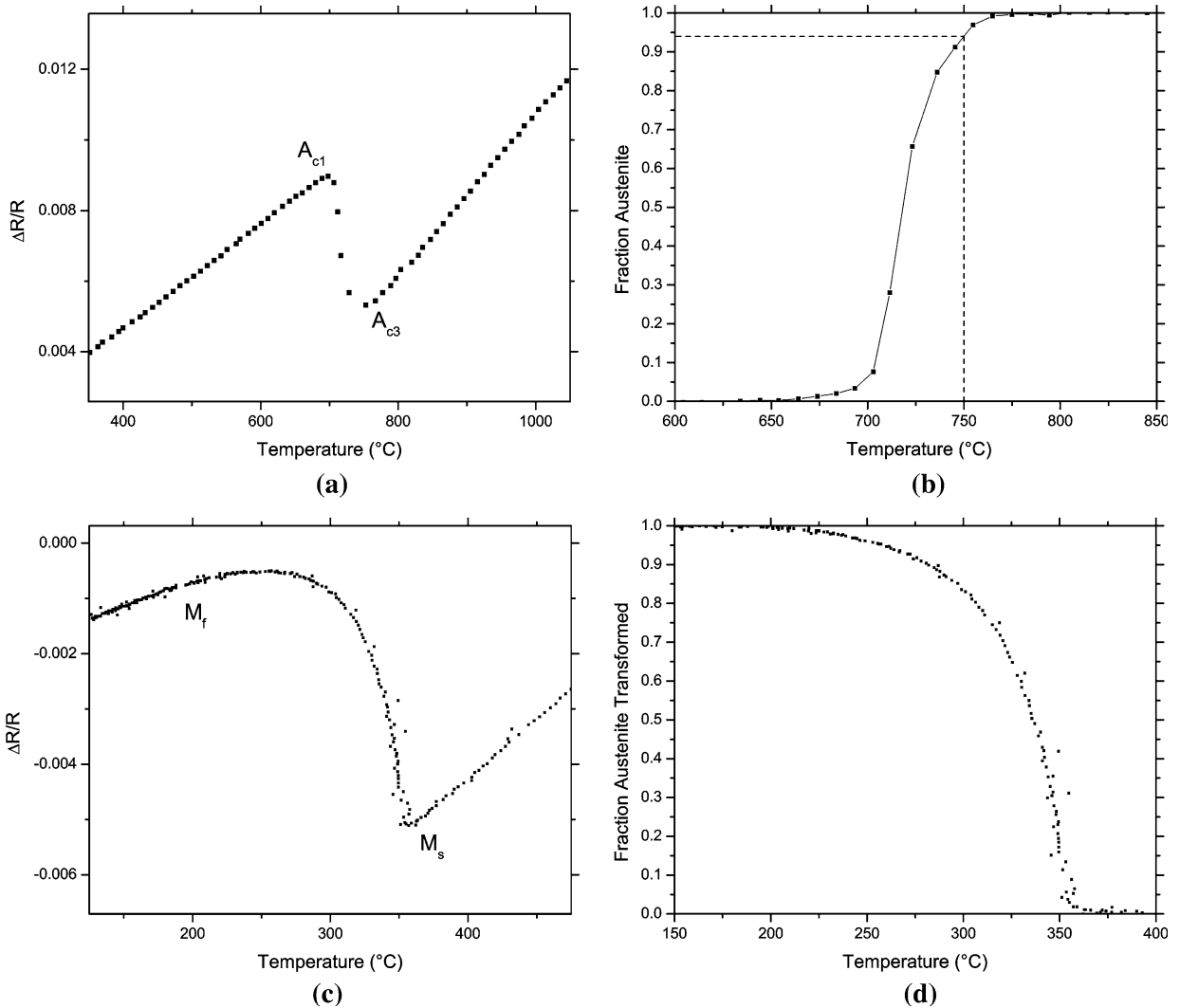


Fig. 6—Acquired dilatometry plots for BA-160 CGHAZ simulations indicating (a) location of A_{c1} and A_{c3} phase transformation temperatures, (b) on-heating austenite volume fraction at 1023 K (750 °C), (c) location of on-cooling martensite phase transformation temperatures, and (d) fraction austenite transformed to martensite as a function of temperature.

of the A_{c1} and A_{c3} temperatures for the selected heating rate of 100 K/s was a requirement for accurate simulation of the characteristic HAZ regions. The locations of the A_{c1} and A_{c3} temperatures are identified in Figure 6(a). The A_{c1} and A_{c3} temperatures were determined by performing a linear fit analysis of the on-heating dilatation data in the region of the austenite transformation. From an average of the FGHAZ and CGHAZ simulations, the A_{c1} and A_{c3} temperatures were determined to be 947 K \pm 10 K (674 °C \pm 10 °C) and 1067 K \pm 10 K (794 °C \pm 10 °C), respectively. Using the method of Eldis,^[32] which is based on the volume change and thermal expansion coefficient, the austenite volume fraction was determined as a function of temperature during the on-heating portion of the thermal cycle (Figure 6(b)). It can be seen that approximately 90 vol pct austenite was formed for the 1023 K (750 °C) peak temperature of the ICHAZ region.

The on-cooling phase transformation temperatures were determined from both dilatometry and SS-DTA analyses. A summary of the on-cooling phase transfor-

mation temperatures are presented in Table V. The martensite transformation was the only austenite decomposition product detected from both dilatometry and SS-DTA analyses. The dilatometry and SS-DTA results were in good agreement, with consistency being found for each of the peak temperatures and cooling rates. The martensite start temperature (M_s) was found to be affected by peak temperature, varying from average values of 605 K (332 °C) in the FGHAZ to 630 K (357 °C) in the CGHAZ. The results suggest the limited effect of cooling rate on the M_s for a given peak temperature. The M_s for the CGHAZ simulations was in best agreement with the 633 K \pm 8.4 K (360 °C \pm 8.4 °C) reported by Saha *et al.*^[5] The higher M_s of the CGHAZ compared to the FGHAZ was unexpected given that more pronounced dissolution during the on-heating portion of the weld thermal cycle is expected in the CGHAZ compared to the FGHAZ. A higher level of chemical elements remaining in austenite solid solution upon cooling would be expected to result in a lower M_s .^[33] The higher M_s of the CGHAZ is not

Table V. Martensite Phase Transformation Temperatures for BA-160 Single-Pass HAZ Simulations

Sample		Transformation Temperature [K (°C)]			
		Dilatometry		SS-DTA	
		M_s	M_f	M_s	M_f
ICHAZ	LHI	617 (344)	448 (175)	624 (351)	444 (171)
	HHI	616 (343)	472 (199)	612 (339)	469 (196)
FGHAZ	LHI	607 (334)	450 (177)	606 (333)	451 (178)
	HHI	602 (329)	469 (196)	603 (330)	467 (194)
CGHAZ	LHI	628 (355)	451 (178)	632 (359)	443 (170)
	HHI	629 (356)	474 (201)	631 (358)	468 (195)

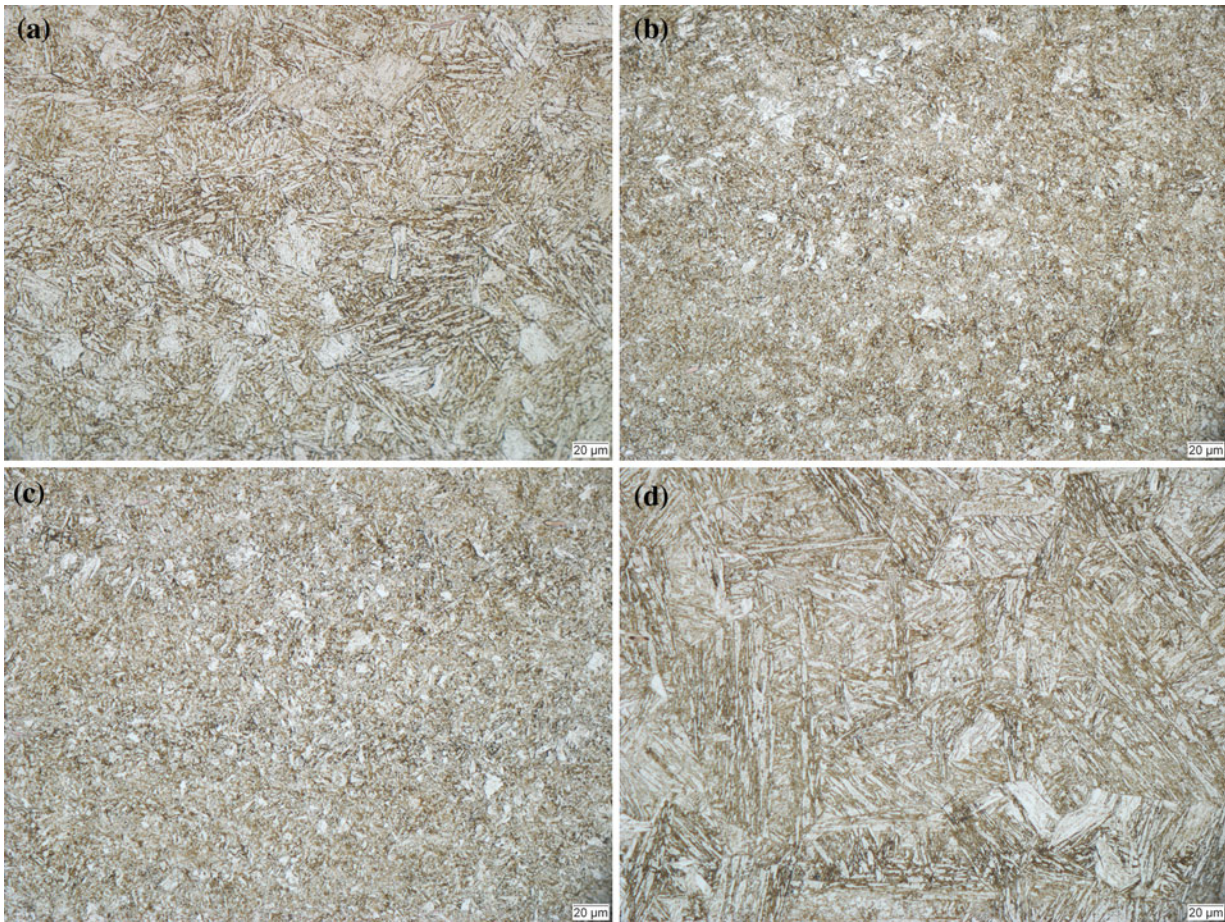


Fig. 7—Representative microstructures of BA-160 single-pass HAZ regions: (a) SCHAZ, (b) ICHAZ, (c) FGHAZ, and (d) CGHAZ.

likely attributed to decarburization of the samples at the higher peak temperature since carbon content is relatively low in BA-160. The lower M_s exhibited by the FGHAZ may be attributed to a finer austenite grain size in the FGHAZ, which is known to affect martensite kinetics and lower the M_s .^[34] The M_f was affected by cooling rate, with the HHI samples exhibiting a higher M_f for each peak temperature simulated. For the SCHAZ samples, negligible on-heating and on-cooling dilatations were detected, confirming the 923 K (650 °C) peak temperature to be below the A_{c1} temperature for the 100 K/s heating rate employed. The absence of a thermal arrest for the SCHAZ simulation (Figure 5)

further suggests that austenite did not form during the on-heating portion of the thermal cycle. Figures 6(c) and (d) exhibit the on-cooling dilatation curve in the region of the martensite phase transformation and the fraction austenite transformed to martensite as a function of temperature.

D. Characterization of Single-Pass HAZ Microstructures

Shown in Figure 7 are representative optical micrographs of the single-pass HAZ microstructures. Each region consists of lath martensite typical in low-carbon

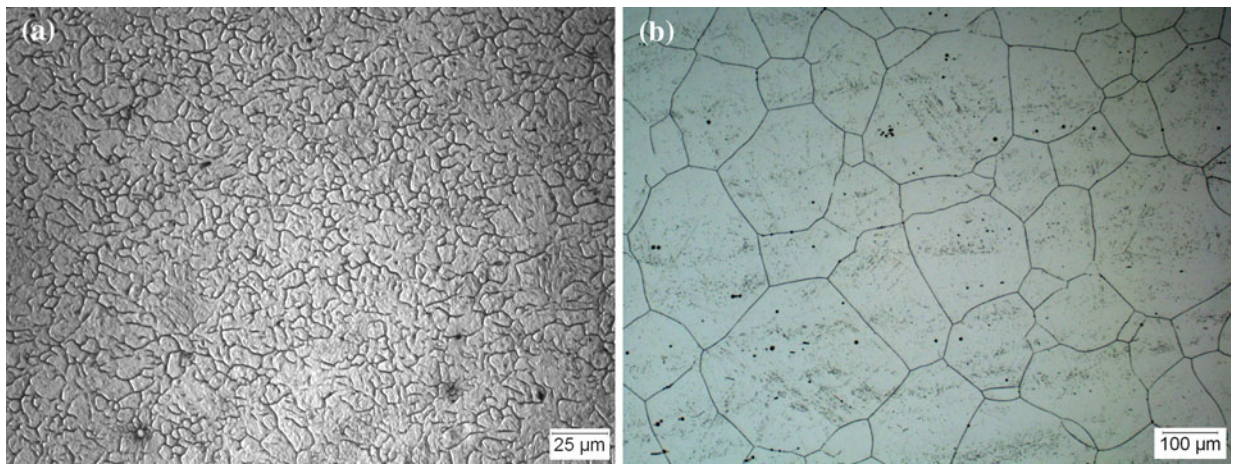


Fig. 8—Prior austenite grains in BA-160 LHI HAZ samples: (a) FGHAZ and (b) CGHAZ.

Table VI. Summary of Average Prior Austenite Grain Diameters in BA-160 Single-Pass HAZ Samples

HAZ Region	Prior Austenite Grain Diameter (μm)
BM/SCHAZ	13.7
ICHAZ	≈ 2
FGHAZ-LHI	4.4
FGHAZ-HHI	5.6
CGHAZ-LHI	71.8
CGHAZ-HHI	103.3

steels. Little difference was observed optically between the LHI and HHI microstructures. Finer microstructures were observed in the ICHAZ and FGHAZ compared to the SCHAZ and CGHAZ regions.

Prior austenite grain size is important in determining both the on-cooling phase transformation behavior and the mechanical properties of the resultant HAZ microstructures. Light optical micrographs of the prior austenite grains in the FGHAZ and CGHAZ regions are shown in Figure 8. A summary of the average prior austenite grain diameters are provided in Table VI. Clearly, a large difference in prior austenite grain size was observed between the ICHAZ and CGHAZ regions. Due to the extremely fine microstructure of the ICHAZ, the prior austenite grain boundaries could not be completely resolved. As such, only an estimated value of approximately $2 \mu\text{m}$ could be determined. Furthermore, a bimodal distribution of grain diameters would be expected in the ICHAZ, provided that not all of the BM microstructure transformed to austenite during the on-heating portion of the thermal cycle.

A plot of Vickers microhardness as a function of peak temperature for the BA-160 simulated HAZ regions is provided in Figure 9. The hardness profile for the HAZ regions is similar for both the LHI and HHI conditions; a slightly higher hardness was observed in the LHI samples for each HAZ region. A peak hardness of 436 HV was observed in the ICHAZ with the lowest hardness of 347 HV occurring in the CGHAZ. The hardness of the SCHAZ and FGHAZ samples was found

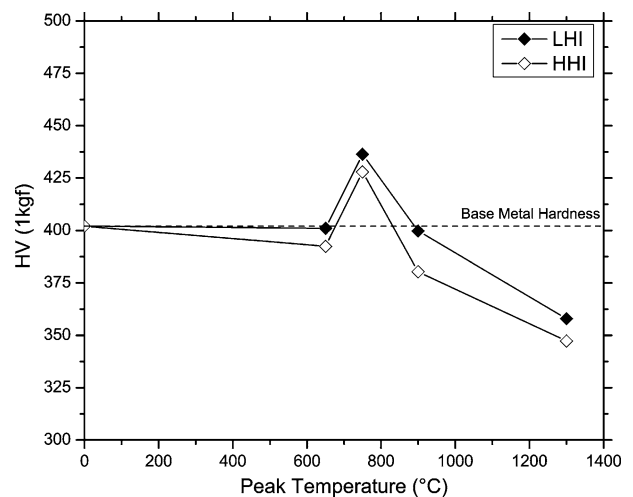


Fig. 9—Vickers microhardness of BA-160 single-pass HAZ regions as a function of peak temperature and heat input conditions.

to be slightly lower than the BM. The hardness profile and measured values of the simulated HAZ samples were in excellent agreement with the as-welded HAZ hardness measurements of the spot weld (Figure 4). This reaffirms the Gleeble HAZ simulation technique as an accurate method to simulate HAZ regions. The hardness profile of the HAZ regions of BA-160 can be considered unusual when referring to the HAZ hardness profiles determined for HSLA-100 naval steel.^[11,12] For HSLA-100, cooling rate dependence leads to different austenite decomposition products (martensite, bainite, ferrite, *etc.*) such that the final microstructure and hardness profile can be a strong function of the peak temperature and cooling rate, *i.e.*, HAZ location and heat input. This leads to an overall different HAZ hardness profile for BA-160 than is observed in steels that transform to various phases on cooling.

Detailed microstructure characterization of the HHI HAZ samples was conducted with the electron backscatter diffraction (EBSD) and atom-probe tomography (APT) techniques. These characterization results were

previously published.^[35] Briefly, the EBSD results were useful in determining the packet and block sizes of the lath martensite, which provided a grain boundary strengthening contribution for each HAZ region.^[36] A significant strengthening difference was determined, attributed to much finer martensite packet, and block sizes in the FGHAZ and ICHAZ compared to the CGHAZ. The APT data revealed that Cu precipitates were shown to coarsen substantially in the SCHAZ, partially dissolve in the ICHAZ, undergo near complete dissolution in the FGHAZ, and reform Cu clusters in the CGHAZ during the on-cooling portion of the thermal cycle. By using quantitative data acquired from the APT experiments, the Cu precipitation strengthening contribution was estimated from the model of Russell and Brown.^[37] The observed HAZ hardness trend exhibited good correlation with the predicted strength increment due to martensite substructure and Cu precipitate strengthening.^[35] Also observed from the APT data were maximum Cu concentrations of 17 and 20 at. pct in the ICHAZ and CGHAZ regions, respectively. The Cu segregation would be expected to decrease the local melting temperature and potentially lead to premature liquation and HAZ liquation cracking susceptibility.

Retained austenite in the CGHAZ microstructure, as shown in Figure 10, was visible as white films along the martensite lath boundaries, a typical form of retained austenite in lath martensite microstructures.^[38] Results obtained from X-ray diffraction tests were inconclusive in determining the amount of retained austenite, similar to what previous researchers reported.^[8,39] *In-situ* time-resolved X-ray diffraction (TRXRD) investigations were performed^[40] on BA-160 steel using the methodology presented elsewhere.^[41] Two peak temperatures above the A_{c3} were chosen to produce coarse (CGHAZ) and fine (FGHAZ) austenite grains. It is noted that the cooling rates were slightly different from the single-pass HAZ simulations. The results from these tests are presented in Figure 11. The data clearly show the presence of fcc diffraction peaks in the FGHAZ sample. However, in the CGHAZ sample, the amount of



Fig. 10—Presence of retained austenite in the BA-160 CGHAZ sample revealed as white films along martensite lath boundaries.

retained austenite upon reaching lower temperatures was insignificant. In order to provide a quantitative evaluation, the individual data collected at the end of the experiments [$T \approx 343$ K (70 °C)] were compared, as shown in Figure 12. The ratio of the fcc to bcc diffraction peaks ($d_{\{111\}_{fcc}}/d_{\{011\}_{bcc}}$) in the FGHAZ sample was calculated to be 0.10. It is important to note that even in the CGHAZ sample there was a small diffraction peak corresponding to the $\{002\}_{fcc}$ planes. The preceding results further show the strong correlation between austenite grain size and martensite kinetics, as proposed elsewhere,^[34] and are consistent with analyses performed more recently on BA-160 using a hybrid characterization technique.^[42] The effect of the amount of retained austenite on the hardness/strength of the HAZ regions is not yet resolved.

E. Continuous Cooling Transformation Diagrams

The HAZ microstructure is a function of both composition and microstructure, and the nature of the weld thermal cycle. A continuous cooling transformation (CCT) diagram for a particular steel can be used to predict microstructure as a function of cooling rate.^[43] Austenite inhomogeneity often occurs in welding due to the inability of alloying elements and precipitates to completely solutionize during the rapid weld thermal cycle. Since the time spent in the austenite region is relatively short, CCT diagrams constructed from short-time holds in the austenite region are more appropriate for determining the HAZ CCT behavior than the conventional CCT procedure of holding on the order of an hour at a temperature slightly above the A_{c3} .^[44,45] To develop experimental CCT diagrams for the FGHAZ and CGHAZ regions, slow cooling experiments were conducted for the 1173 K and 1573 K (900 °C and 1300 °C) peak temperatures. Samples were control cooled at an exponential rate such that the average cooling rate in the 1073 K to 773 K (800 °C to 500 °C) range was 1 K/s, *i.e.*, $t_{8/5}$ of 300 seconds. In both cases, the only on-cooling phase transformation detected was martensite, suggesting it to be the only austenitic decomposition product for even the slowest cooling rates expected in the HAZ. The two experimental HAZ CCT diagrams are presented in Figure 13.

To compare the experimental findings with materials modeling predictions, CCT diagrams for BA-160 were calculated with the JMatPro 5.1 software (Sente Software Ltd., Surrey, UK). JMatPro is commercially available software designed to calculate the properties and behavior of multicomponent alloys.^[46] The predicted TTT and CCT diagrams for steels are derived from the chemical composition, austenitization temperature, and austenite grain size.^[47] The incorporated phase transformation model is based on the model of Kirkaldy *et al.*^[48] and validated with experimentally determined TTT and CCT diagrams.^[49–51] The calculated CCT diagrams are presented in Figure 14. For a peak temperature of 1573 K (1300 °C) in the CGHAZ, the formation of bainite is predicted only for cooling rates (<1 K/s) slower than those expected in a weld thermal cycle. For a peak temperature of 1173 K

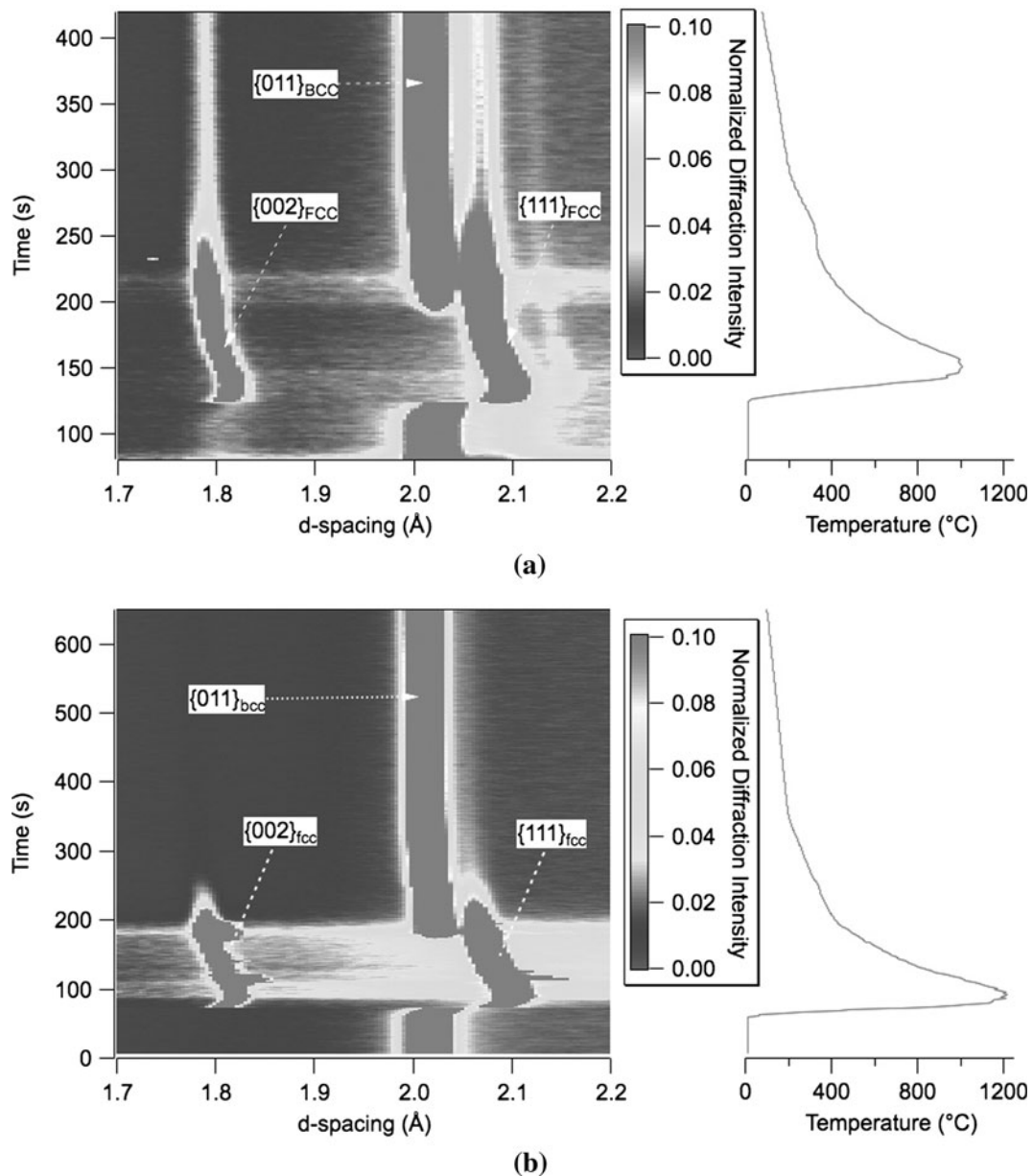


Fig. 11—Overview of the in-situ TRXRD data from samples representing the (a) FGHAZ and (b) CGHAZ. The noise in the fully austenite region of the FGHAZ simulation is lower than for the CGHAZ due to its finer austenite grain size, which leads to good diffraction intensity.

(900 °C) in the FGHAZ, the formation of bainite is predicted for moderate weld cooling rates (>10 K/s). The predicted M_s of 603 K (330 °C) was in good agreement with experimentally determined values.

It can be seen that the high hardenability of BA-160 promotes the formation of martensite at relatively slow cooling rates. As a result, a completely martensitic microstructure can be expected for a wide range of weld process parameters. This also leads to simplicity in microstructural predictions for a wide weld process parameter window.

F. Impact Toughness of Single-Pass HAZ Regions

Provided in Table VII are the Charpy V-notch impact energy test results. The adjusted value of 136 J for the

BM at 293 K (20 °C) is below the 176 J peak value that was reported by Saha *et al.* for standard size Charpy specimens.^[5] However, it is in accordance with the 136 J baseline toughness value at ambient temperature. The adjusted value of 118 J for the BM at 223 K (−50 °C) is in good agreement with the 120 J that was previously reported for a test temperature of 223 K (−50 °C). Comparative test results for the HAZ regions reveal better impact toughness than the BM at both test temperatures. The highest toughness was exhibited by the CGHAZ, where values of 179 and 180 J were achieved at 293 K and 223 K (20 °C and −50 °C), respectively. While the BM and SCHAZ regions exhibited decreased toughness at the lower testing temperature, negligible differences were observed for the ICHAZ, FGHAZ, and CGHAZ regions. The overall

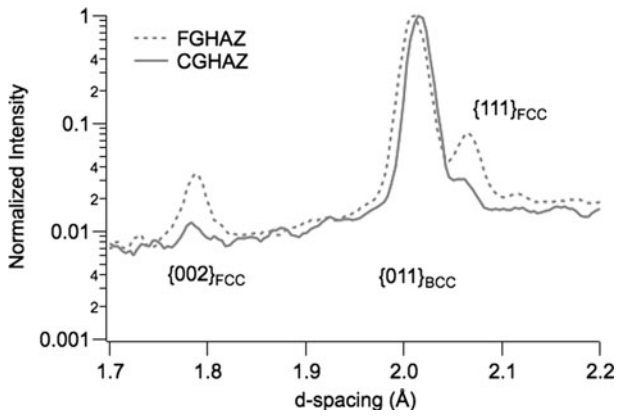


Fig. 12—Comparison of the diffraction spectra from FGHAZ and CGHAZ samples showing the substantial presence of fcc diffraction intensity. The y-axis is presented in logarithmic scale to delineate the austenite peaks.

toughness values of the ICHAZ, FGHAZ, and CGHAZ regions were also inversely correlated with their measured hardness values.

Representative SEM micrographs of the fracture surfaces of BA-160 BM and CGHAZ impact test samples are shown in Figure 15. A predominant quasi-cleavage mode of fracture is evident for the BM sample tested at 223 K (−50 °C), correlating with the reduced impact energy exhibited at the lower temperature. The CGHAZ fracture surfaces exhibited predominantly ductile microvoid coalescence at both test temperatures.

The overall results suggest that a toughness loss in the HAZ of an actual weld would not be expected for the temperature range evaluated. The maintenance of good toughness in the HAZ regions at low temperatures can be partially attributed to the formation of retained austenite in the HAZ microstructures, which was shown to have a beneficial effect on toughness.^[52–54] The

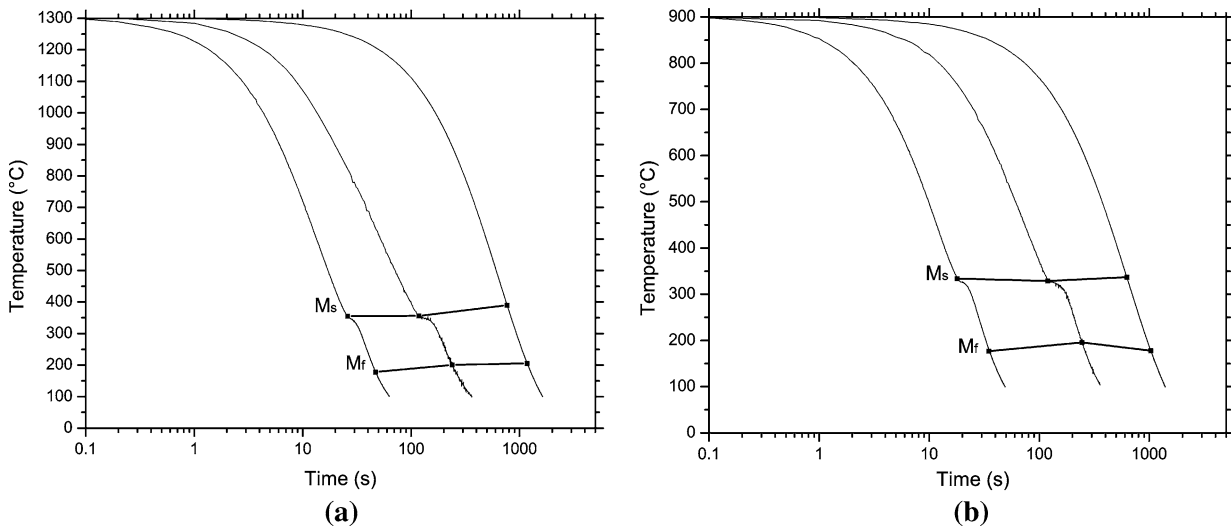


Fig. 13—Experimental BA-160 HAZ CCT diagrams for (a) CGHAZ and (b) FGHAZ.

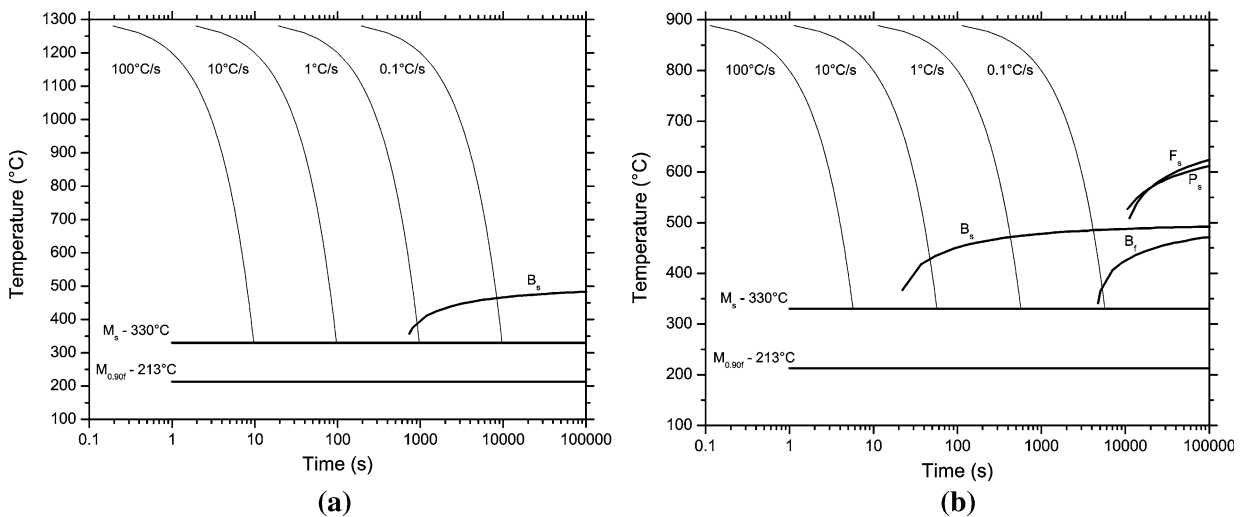


Fig. 14—CCT diagrams of BA-160 calculated with JMatPro software for (a) 1573 K (1300 °C) austenitization temperature and 100- μ m austenite grain diameter and (b) 1173 K (900 °C) austenitization temperature and 5- μ m austenite grain diameter.

benefits of retained austenite were attributed to it acting as a sink for elements deleterious to fracture toughness such as carbon, and in disrupting the crystallographic alignment of the martensite packets.^[55] Thermally stable austenite that is formed along martensite lath boundaries (Figure 10) acts to interrupt the crystallographic alignment of the laths within the martensite packets,

preventing cooperative transpacket cleavage.^[56] Furthermore, Ni is known to lower the ductile-to-brittle transition temperature in steels by providing good resistance to cleavage fracture and promoting the cross-slip of screw dislocations.^[57,58] Recent research on the toughness of low-carbon lath martensite identified the unit crack path for cleavage fracture as being the packet.^[59] Thus, the finer packet size in the ICHAZ and FGHAZ regions would be expected to provide better toughness than the CGHAZ at temperatures below those investigated in this study.

Currently, research has not established a correlation between the amount of retained austenite and impact toughness. The TRXRD experiments clearly indicated a higher amount of retained austenite in the FGHAZ than the CGHAZ. The higher toughness exhibited by the CGHAZ and the preliminary TRXRD results suggests that a strong correlation between the amount of retained austenite and impact toughness across the various HAZ regions does not exist in BA-160. A detailed investigation of the amount of retained austenite and its effect on the HAZ properties is a part of the ongoing research.

Table VII. Summary of Charpy V-Notch Impact Test Results for BA-160 Single-Pass HAZ Samples

Region	E_{avg}, E_{adj} Impact Energy (J)	
	Test Temperature [K (°C)]	
	293 (20)	223 (-50)
BM	16.9, 136	14.7, 118
SCHAZ	18.5, 148	16.1, 129
ICHAZ	18.5, 148	18.8, 150
FGHAZ	20.7, 165	20.2, 161
CGHAZ	22.4, 179	22.5, 180

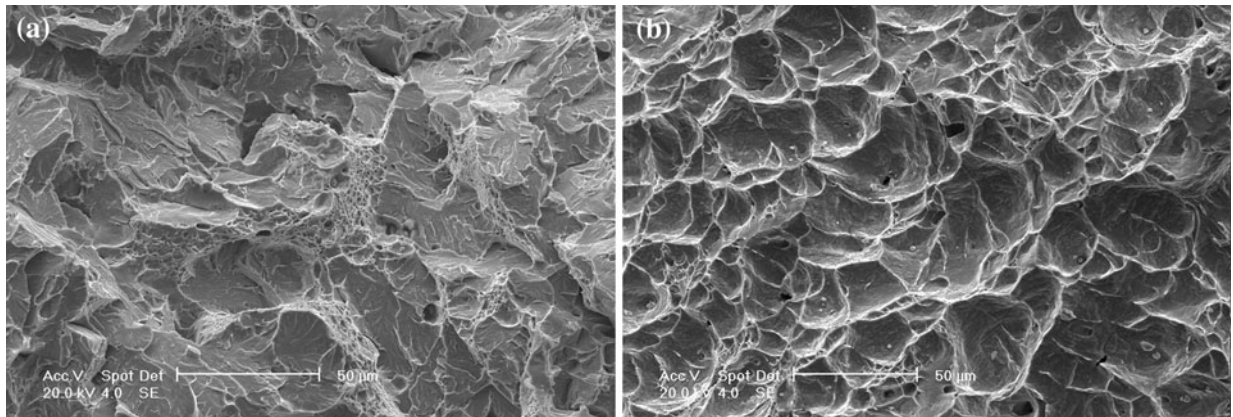


Fig. 15—SEM photomicrographs of BA-160 Charpy V-notch impact samples tested at 223 K (-50 °C): (a) BM and (b) CGHAZ.

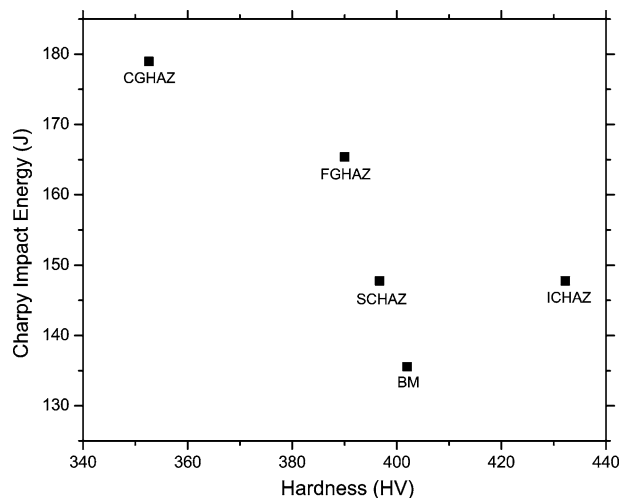


Fig. 16—Plot of Charpy impact energy values vs average Vickers microhardness of single-pass HAZ regions. Lower hardness was correlated with higher toughness except for the ICHAZ.

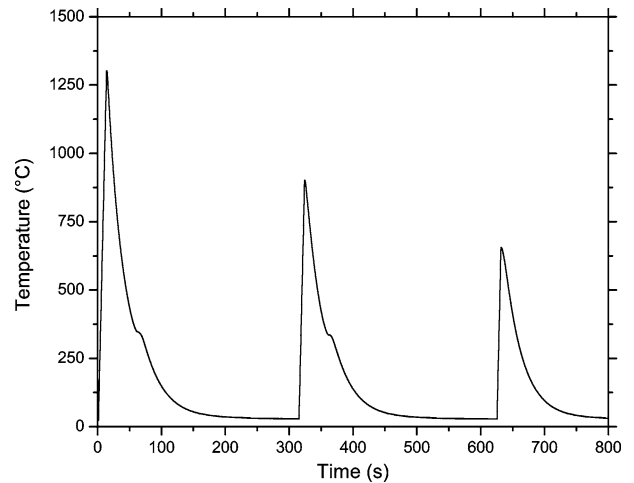


Fig. 17—Acquired thermal profile of BA-160 triple-pass CG + FG + SC HAZ simulation.

Table VIII. Martensite Phase Transformation Temperatures for BA-160 Multipass HAZ Simulations as Determined by Dilatometry

Sample	Simulation	Transformation Temperature [K (°C)]	
		M_s	M_f
CG + FG	CG	626 (353)	465 (192)
	FG	618 (345)	450 (177)
CG + IC	CG	625 (352)	448 (175)
	IC	624 (351)	457 (184)
CG + SC	CG	628 (355)	451 (178)
CG + FG + SC	CG	629 (356)	—
	FG	625 (352)	—

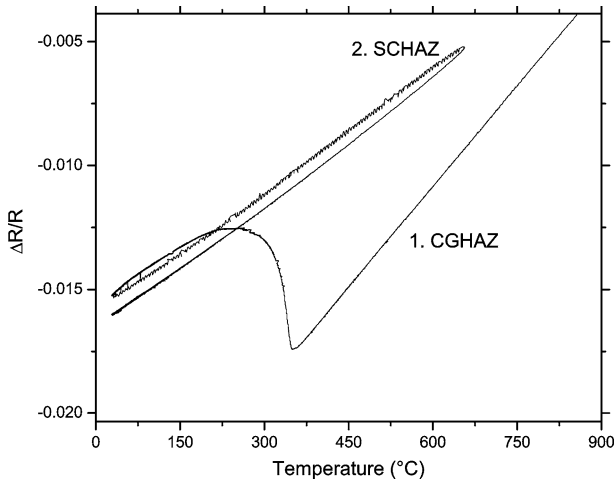


Fig. 18—Acquired dilatometry plot of BA-160 double-pass CG + SC HAZ simulation showing the location of the M_s and M_f for the initial CGHAZ simulation. The data indicate that austenite did not form in the secondary SCHAZ simulation.

In Figure 16, the adjusted impact energy values determined at 293 K (20 °C) are plotted against the average hardness values of the single-pass HAZ regions. The hardness-toughness plot shows that lower hardness correlated with higher impact toughness except for the ICHAZ, which exhibited both a hardness and toughness increase compared to the BM. The better overall properties exhibited by the ICHAZ suggest that the BM heat treatment could be further evaluated to produce an optimal combination of strength and toughness.

G. Microstructural Response to Multipass HAZ Simulations

Shown in Figure 17 is the acquired thermal history for the CG + FG + SC HAZ simulation of BA-160. Overall, good correlation was found for the M_s and M_f phase transformation temperatures of the multipass HAZ regions when compared to the single-pass HAZ regions. A summary of the transformation temperatures, as determined by dilatometry, are provided in Table VIII. The M_f temperatures could not be accurately determined for the CG + FG + SC sample.

Consistent with the findings of the single-pass SCHAZ simulations, negligible on-heating and on-cooling dilatations were detected during the SCHAZ simulation of the CG + SC HAZ simulation (Figure 18).

Optical micrographs of the BA-160 multipass HAZ samples are shown in Figure 19. Microstructure refinement was evident in the CG + FG and CG + IC HAZ regions when compared to the single-pass CGHAZ microstructure (Figure 19(d)). As expected from the dilatation data, the CG + SC HAZ exhibited a similar microstructure compared to the CGHAZ since new austenite grains were not formed during the secondary thermal cycle. Similarly, comparable microstructures were observed for the CG + FG and CG + FG + SC HAZ samples.

The average microhardness values of the multipass HAZ samples are summarized in Table IX. For all regions simulated, an increase in hardness was observed compared to the single-pass CGHAZ region. The hardness values of the double-pass HAZ regions were shown to increase according to the second HAZ simulation offering the higher single-pass HAZ hardness (ICHAZ > SCHAZ > FGHAZ). This indicates that the strengthening is dominated by the second thermal cycle. The highest hardness was found to be 423 HV for the triple-pass CG + FG + SC HAZ region. When considering the EBSD and APT characterization results of the single-pass HAZ regions,^[35] the increase in hardness in the CG + FG + SC region can be attributed to both lath martensite refinement during the second FGHAZ simulation and Cu re-precipitation during the third SCHAZ simulation. The measured hardness of the CG + FG + SC HAZ region was also higher than for any of the three individual single-pass HAZ regions. Overall, the hardness values of the multipass HAZ regions were found to be in a narrower range compared to the single-pass HAZ regions. A narrower range of hardness values resulting from multipass welding is viewed positively in terms of weldability. Furthermore, while the multipass HAZ simulations were not an exhaustive investigation, the results do suggest that a HAZ hardness decrease is not expected in multipass welding.

IV. CONCLUSIONS

1. Microstructural evidence of the weld solidification substructure of BA-160 suggested fcc austenite as the primary solidification phase. The solidification grain boundaries of the FZ were observed to link up with the prior austenite grain boundaries near the weld interface, suggesting the formation of a PMZ and possible susceptibility to HAZ liquation cracking. A hardness variation of approximately 100 HV was observed across the HAZ, increasing from a minimum of 353 HV in the CGHAZ to a maximum of 448 HV in the ICHAZ. The average hardness of the FZ was 364 HV.
2. After a two-step PWHT of the spot weld, hardness increases were observed in the FZ, CGHAZ, and FGHAZ regions, while negligible differences were observed in the ICHAZ, SCHAZ, and BM regions.

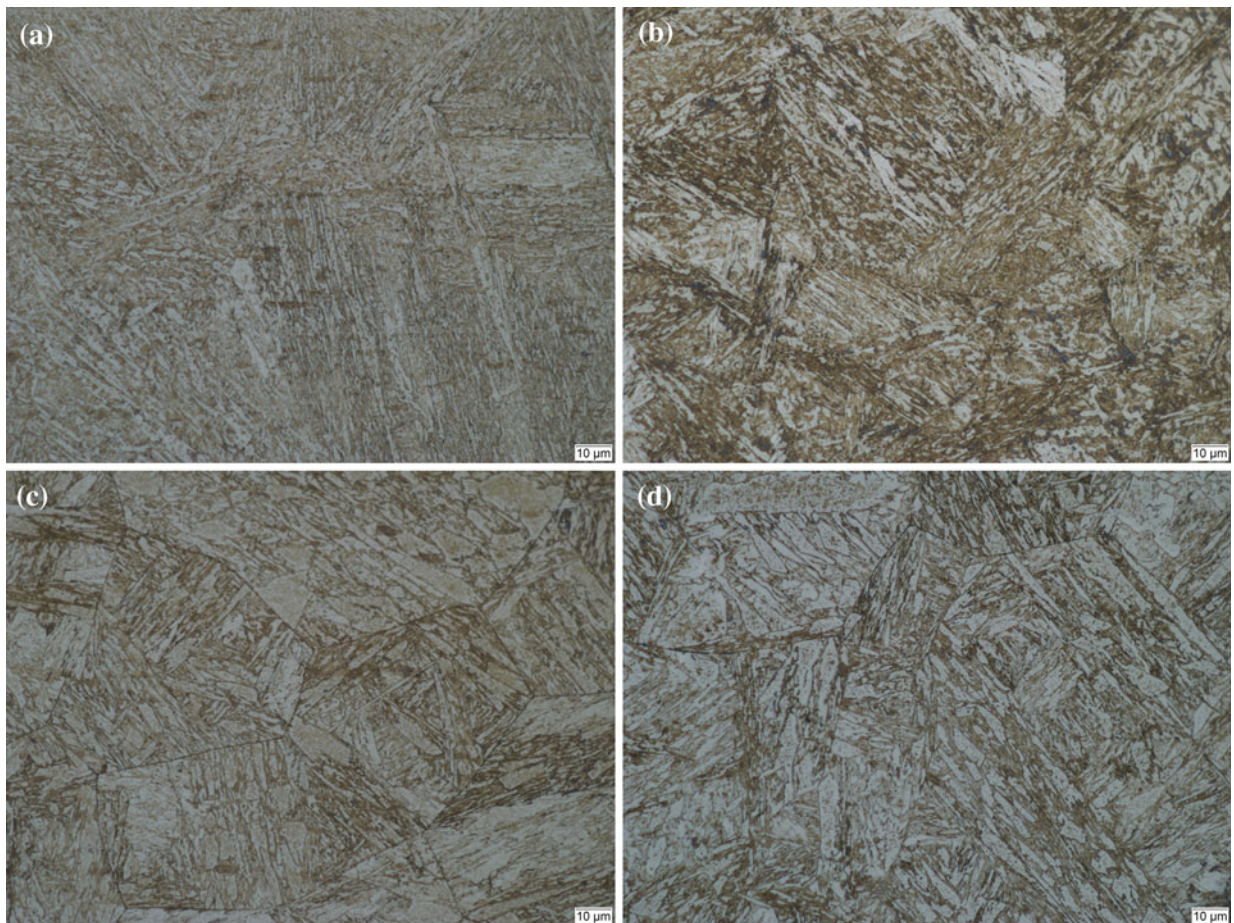


Fig. 19—Microstructures of BA-160 simulated multipass HAZ regions: (a) CG + FG, (b) CG + IC, (c) CG + SC, and (d) single-pass CGHAZ shown for comparison.

Table IX. Summary of Average Vickers Microhardness Values for BA-160 Multipass HAZ Samples

HAZ Region	Vickers Microhardness
CG + FG	384
CG + IC	416
CG + SC	406
CG + FG + SC	423

Overall, a smaller variation of hardness was observed after PWHT when compared to the as-welded condition.

- The dilatometry and SS-DTA phase transformation techniques employed during the single-pass HAZ simulations determined martensite to be the only austenite transformation product in the HAZ for a wide range of cooling rates. The M_s was shown to be dependent on HAZ peak temperature, varying from average values of 605 K (332 °C) in the FGHAZ to 630 K (357 °C) in the CGHAZ. This observation provides further evidence of the effect of austenite grain size on martensite kinetics. The M_f ranged from 443 K to 474 K (170 °C to 201 °C) and exhibited cooling rate dependence; lower values were measured for the LHI simulations.

- Similar HAZ hardness profiles were measured for both the LHI and HHI simulations, with higher hardness being observed for the LHI samples. The maximum hardness of 436 HV and minimum hardness of 347 HV were observed in the ICHAZ and CGHAZ regions, respectively. Slight hardness decreases were observed in both the SCHAZ and FGHAZ regions when compared to the BM hardness of 402 HV.
- The single-pass HAZ regions consisted of a lath martensite microstructure that was dependent on prior austenite grain size. A significant difference in prior austenite grain diameter was measured throughout the HAZ, varying from a maximum of 103 μm in the CGHAZ to a minimum of approximately 2 μm in the ICHAZ. The presence of retained austenite was revealed optically as films along the martensite lath boundaries. *In-situ* TRXRD experiments detected a greater amount of retained austenite in the FGHAZ compared to the CGHAZ.
- Single-pass HAZ regions exhibited higher subsized Charpy V-notch impact toughness than the BM at test temperatures of 293 K and 223 K (20 °C and -50 °C). The highest toughness at both temperatures was exhibited by the CGHAZ, with fracture-volume adjusted values of 179 J at 293 K (20 °C) and 180 J

at 223 K (−50 °C). Lower hardness correlated with higher impact toughness except for the ICHAZ, which exhibited both a hardness and toughness increase compared to the BM.

7. Multipass HAZ regions employing an initial CGHAZ simulation exhibited an increase in hardness compared to the single-pass CGHAZ region. The hardness ranged from 384 HV in the CG + FG HAZ region to 423 HV in the CG + FG + SC HAZ region. The double-pass HAZ hardness values increased according to the second HAZ simulation offering the higher single-pass HAZ hardness (ICHAZ > SCHAZ > FGHAZ).

ACKNOWLEDGMENTS

Funding for this research was provided by the ONR under Grant Award No. N000140811000, Dr. Julie Christodoulou, grant officer. The collaborative efforts of Mr. Xinghua Yu toward the microstructural characterization of simulated HAZ samples were greatly appreciated. The assistance of Drs. Michael Santella and Eliot Specht, Oak Ridge National Laboratory, with the time-resolved X-ray diffraction experiments is also acknowledged.

REFERENCES

1. M.D. Uchic: *J. Mater.*, 2006, vol. 58, p. 24.
2. G. Spanos: *Scripta Mater.*, 2006, vol. 55, p. 3.
3. G. Spanos, A.B. Geltmacher, A.C. Lewis, J.F. Bingert, M. Mehl, D. Papaconstantopoulos, Y. Mishin, A. Gupta, and P. Matic: *Mater. Sci. Eng. A*, 2007, vols. 452–453, pp. 558–68.
4. A. Saha and G.B. Olson: *J. Comput.-Aided Mater. Des.*, 2007, vol. 14, pp. 177–200.
5. A. Saha, J. Jung, and G.B. Olson: *J. Comput.-Aided Mater. Des.*, 2007, vol. 14, pp. 201–33.
6. *Adv. Mater. Processes*, 2004, vol. 162 (12), pp. 9–10.
7. J. Huergo: Office of Naval Research Press Release, Office of Naval Research, Arlington, VA, 2004.
8. M.D. Mulholland and D.N. Seidman: *Scripta Mater.*, 2009, vol. 60, pp. 992–95.
9. Ø. Grong: *Metallurgical Modelling of Welding*, 2nd ed., The Institute of Materials, Cambridge, United Kingdom, 1997, pp. 4–14.
10. K. Easterling: *Introduction to the Physical Metallurgy of Welding*, Butterworth-Heinemann, Oxford, United Kingdom, 1992, pp. 126–27.
11. G. Spanos, R.W. Fonda, R.A. Vandermeer, and A. Matuszeski: *Metall. Mater. Trans. A*, 1995, vol. 26A, pp. 3277–93.
12. M. Shome, O.P. Gupta, and O.N. Mohanty: *Metall. Mater. Trans. A*, 2004, vol. 35A, pp. 985–96.
13. W. Sperko: *Weld J.*, 2005, vol. 84, pp. 37–40.
14. B.T. Alexandrov and J.C. Lippold: *Weld. World*, 2007, vol. 51, pp. 48–59.
15. *Standard Practice for Quantitative Measurement and Reporting of Hypoeutectoid Carbon and Low-Alloy Steel Phase Transformations*, ASTM Designation A 1033–04, ASTM, West Conshohocken, PA, 2004.
16. T. Kop, J. Sietsma, and S. Van der Zwaag: *J. Mater. Sci.*, 2001, vol. 36, pp. 519–26.
17. *Standard Test Methods for Notched Bar Impact Testing of Metallic Materials*, ASTM Designation E 23–07, West Conshohocken, PA, 2007.
18. G.E. Lucas, G.R. Odette, J.W. Shekherd, P. McConnell, and J. Perrin: *The Use of Small-Scale Specimens for Testing Irradiated Material*, ASTM STP 888, Philadelphia, PA, 1986, pp. 305–24.
19. W.R. Corwin and A.M. Houglund: *The Use of Small-Scale Specimens for Testing Irradiated Material*, ASTM STP 888, Philadelphia, PA, 1986, pp. 325–38.
20. G.F. Vander Voort: *Metallography: Principles and Practice*, ASM INTERNATIONAL, Materials Park, OH, 1999, p. 638.
21. A.K. De, J.G. Speer, and D.K. Matlock: *Adv. Mater. Processes*, 2003, vol. 161, pp. 27–30.
22. *Standard Test Methods for Determining Average Grain Size*, ASTM Designation E 112–96, ASTM, West Conshohocken, PA, 1996.
23. *Standard Test Method for Microindentation Hardness of Materials*, ASTM Designation E 384–08, ASTM, West Conshohocken, PA, 2008.
24. J.C. Lippold and D.J. Kotecki: *Welding Metallurgy and Weldability of Stainless Steels*, John Wiley & Sons, Hoboken, NJ, 2005, p. 154.
25. B. Sundman, B. Jansson, and J.-O. Andersson: *CALPHAD*, 1985, vol. 9, pp. 153–90.
26. J.C. Lippold, W.A. Baeslack, and I. Varol: *Weld. J.*, 1992, vol. 71, pp. 1s–14s.
27. C.S. Smith and E.W. Palmer: *Trans. TMS-AIME*, 1933, vol. 105, pp. 133–68.
28. E. Hornbogen and R.C. Glenn: *Trans. TMS-AIME*, 1960, vol. 218, pp. 1064–70.
29. S.R. Goodman, S.S. Brenner, and J.R. Low: *Metall. Trans.*, 1973, vol. 4, pp. 2363–69.
30. S.R. Goodman, S.S. Brenner, and J.R. Low: *Metall. Trans.*, 1973, vol. 4, pp. 2371–78.
31. M.S. Gagliano and M.E. Fine: *Metall. Mater. Trans. A*, 2004, vol. 27A, pp. 2323–29.
32. G. Eldis: *Hardenability Concepts with Applications to Steel*, AIME, New York, NY, 1978, pp. 126–57.
33. G. Krauss: *Steels: Processing, Structure, and Performance*, ASM INTERNATIONAL, Materials Park, OH, 2005, p. 64.
34. H.-S. Yang and H.K.D.H. Bhadeshia: *Scripta Mater.*, 2009, vol. 60, pp. 493–95.
35. X. Yu, J.L. Caron, S.S. Babu, J.C. Lippold, D. Isheim, and D.N. Seidman: *Acta Mater.*, 2010, vol. 58, pp. 5596–5609.
36. J.P. Naylor: *Metall. Trans. A*, 1979, vol. 10A, pp. 861–73.
37. K.C. Russell and L.M. Brown: *Acta Metall.*, 1972, vol. 20, pp. 969–74.
38. H. Lippard: Ph.D. Dissertation, Northwestern University, Evanston, IL, 1999.
39. A. Saha: Ph.D. Dissertation, Northwestern University, Evanston, IL, 2004.
40. S.S. Babu, M.L. Santella, X. Yu, J.L. Caron, and E.D. Specht: The Ohio State University, Columbus, OH, unpublished research, 2010.
41. S.S. Babu, E.D. Specht, S.A. David, J. Karapetrova, P. Zschak, M. Peet, and H.K.D.H. Bhadeshia: *Metall. Mater. Trans. A*, 2005, vol. 36A, pp. 985–96.
42. X. Yu, S.S. Babu, J.C. Lippold, H. Terasaki, and Y. Komizo: *Metall. Mater. Trans. A*, 2011, vol. 42A, DOI: [10.1007/s11661-011-0746-4](https://doi.org/10.1007/s11661-011-0746-4).
43. G. Krauss: *Steels: Processing, Structure, and Performance*, ASM INTERNATIONAL, Materials Park, OH, 2005, pp. 184–94.
44. P.L. Harrison and R.A. Farrar: *Int. Mater. Rev.*, 1989, vol. 34, pp. 35–51.
45. M. Shome and O.N. Mohanty: *Metall. Mater. Trans. A*, 2006, vol. 37A, pp. 2159–69.
46. N. Saunders, Z. Guo, X. Li, A.P. Miodownik, and J.-P. Schillé: *J. Mater.*, 2003, vol. 55, pp. 60–65.
47. N. Saunders, Z. Guo, X. Li, A.P. Miodownik, and J.-P. Schillé: *The Calculation of TTT and CCT Diagrams for General Steels*, Thermotech, Guildford, United Kingdom.
48. J.S. Kirkaldy, B.A. Thomson, and E.A. Baganis: *Hardenability Concepts with Applications to Steel*, AIME, New York, NY, 1978, pp. 82–125.
49. *Atlas of Isothermal Transformation Diagrams of B.S. En Steels*, Iron and Steel Institute, London, 1956.
50. H.E. Boyer: *Atlas of Isothermal and Cooling Transformation Diagrams*, ASM, Metals Park, OH, 1977.
51. M. Atkins: *Atlas of Continuous Cooling Transformation Diagrams for Engineering Steels*, ASM, Metals Park, OH, 1977.

52. S.-K. Hwang, J. Sungho, and J.W. Morris: *Metall. Trans. A*, 1975, vol. 6A, pp. 2015–21.
53. J.I. Kim and J.W. Morris: *Metall. Trans. A*, 1980, vol. 11A, pp. 1401–06.
54. H. Nakagawa, T. Miyazaki, and H. Yokota: *J. Mater. Sci.*, 2000, vol. 35, pp. 2245–53.
55. J.I. Kim and J.W. Morris: *Metall. Trans. A*, 1981, vol. 12A, pp. 1957–63.
56. J.I. Kim, C.K. Syn, and J.W. Morris: *Metall. Trans. A*, vol. 14A, pp. 93–103.
57. L.-Å. Norström and O. Vingsbo: *Met. Sci.*, 1979, vol. 13, pp. 677–84.
58. W.C. Leslie: *The Physical Metallurgy of Steels*, Hemisphere Publishing Corporation, New York, NY, 1981, pp. 302–03.
59. C. Wang, M. Wang, J. Shi, W. Hui, and H. Dong: *Scripta Mater.*, 2008, vol. 58, pp. 492–95.